A 2D volume conservative numerical model of hydraulic fracturing

Magnus Wangen

Institute for Energy Technology, P.O.Box 40, N-2027 Kjeller, Norway

Abstract

A volume conservative numerical approach is suggested for the modelling of propagation of a hydraulic fracture away from an injection well. A regular finite element grid is applied at the reservoir scale without any special gridding of the fracture. Models for critical fluid pressure are used to derive exact solutions for the propagation of hydraulic fractures in impermeable and homogeneous rocks. The numerical model is verified by these exact solutions for hydraulic fracturing. Numerical examples of hydraulic fracturing of permeable and inhomogeneous rocks are given, where the volume balance is given as a function of time.

Keywords: Hydraulic fracturing, volume conservation, critical fluid pressure, benchmarking, intermittent propagation

1. Introduction

Hydraulic fracturing is rupturing of rocks by injection of fluid under high pressure, and it has become an important process in the production of gas and oil from shale formations (Turcotte et al., 2014). Hydraulic fracturing is also applied in a number of other subsurface operations like the stimulation of oil and gas production from traditional reservoirs (Mack and Warpinski, 2000), in well testing (Zoback, 2010) and in the development of geothermal sites (Baisch et al., 2010).

One of the first models of hydraulic fracturing was suggested by Khristianovic and Zheltov (Khristianovic and Zheltov, 1955), who considered the width of a linear vertical fracture, when the width is the same in the vertical direction. The model of Khristianovic and Zheltov (Khristianovic and Zheltov, 1955) was improved by Geertsma

and de Klerk (Geertsma and de Klerk, 1969) by including fluid loss, and they provided approximations for the fracture length and width as a function of time. This model is often referred to as the GDK-model. Perkins and Kern (1961) suggested a different approach to linear vertical fractures, where the vertical cross section of the fracture is assumed elliptical. This approach was considerable improved by Nordgren (1972) who added fluid loss to the Perkins and Kern model, and obtained analytical and numerical results for the fracture width, length and volume as a function of time. The latter model is known under the name PKN-model. The PKN-model and related models continue to be an area of active research (Kovalyshen and Detournay, 2010). Charlez (1997) presents the mechanical principles of hydraulic fracturing, explains both the PKN- and GDK-models, and discuss the assumptions they build on.

A number of different approaches have been developed for the modelling of hydraulic fracturing, following the first analytical and semi-analytical models. They differ by the way they treat the porous rock, the conditions for fracturing, boundary conditions, spatial dimension, numerical methods, size of the computational domain, how heterogeneities are introduced and assumptions related to fluid flow in the fracture (Charlez, 1997; Mack and Warpinski, 2000; Adachi et al., 2007).

Tzschichholz et al. (1994); Tzschichholz and Herrmann (1995) represented heterogeneities in a porous material by a grid of "welded" beams in order to study the intermittent nature of hydraulic fracturing. Tzschichholz and Wangen (1998) added fluid flow to the beam approach and simulated fluid flow in the fracture and leak-off into the porous medium. A solid medium of springs have also been suggested as a basis for modelling hydraulic fracturing (Flekkøy et al., 2002). The commercial simulator UDEC has been used in studies of the hydraulic fracturing in discrete fracture networks (Riahi and Damjanac, 2013). UDEC simulates propagation of a fracture along predefined planes, where flow occurs inside the fracture (Riahi and Damjanac, 2013). Discrete fracture models (DFM) have been developed into 2D embedded fracture models (EFM), where the fracture system and the surrounding matrix are treated as two separate, but coupled, computational domains (Norbeck and Horne, 2014; Norbeck et al., 2016). The coupling between the fracture- and matrix domains is handled by source terms in a manner similar to the dual porosity model (Norbeck and Horne,

2014). Wheeler et al. (2014); Lee et al. (2016) have developed a continuum approach to fluid driven fracture propagation based on poroelasticity, where the fracture is represented by a phase-field. The phase-field variable is a measure of the local damage of the material, and it is continuous from 0 to 1, where 0 is the fracture and 1 is the rock. This approach uses grid refinement around the fracture and the method is tested in 3D (Lee et al., 2016). The commercial code PFC3D has been used to simulate hydraulic fracturing of an assemblage of grains. The grain contacts have normal and shear forces, which allows for slip, breaking and studies of acoustic emission (Shimizu et al., 2011). Common for these numerical approaches is that they account for heterogeneities and how heterogeneities affect the fracturing process. It should also be mentioned that hydraulic fracturing is modelled with invasion percolation models, where the mechanics of breaking and the fluid flow are represented by simple rules (Norris et al., 2014). These models are applied to rocks where the fracturing process is dominated by heterogeneities. Even though invasion percolation models are based on simple rules they are able to produce realistic microseismic event distributions (Norris et al., 2014).

The model proposed in this article assumes that the rock follows Biot's poroelasticity. The poro-elastic equations for fluid flow and mechanics can be solved decoupled in an unconditionally stable manner, when the mechanics problem is solved with the finite element method and then the flow problem is solved with a cell centered finite difference or finite volume method (Kim et al., 2011a,b). It is therefore possible to couple reservoir simulators with simulators for geomechanics (Settari and Walters, 2001; Rutqvist, 2011; Ganis et al., 2014). The simulators for geomechanics can be extended with modules for fracturing as demonstrated by Ji and Sullivan (2009). Simulators with fully coupled reservoir flow, geomechanics and hydraulic fracturing have also been developed (Dean and Schmidt, 2009).

Wangen (2011, 2013) demonstrated simulation approaches for hydraulic fracturing in 2D and 3D, respectively, where both the poro-elastic fluid flow and the mechanics problem were solved with the finite element method. The fracture was represented with a regular grid at the reservoir scale without any special gridding. The condition for fracture propagation was given as strength assigned to each element in terms of stress or strain limits.

The current work is a continuation of the approach based on a regular finite element grid (Wangen, 2011, 2013). The fluid flow in the fracture, during intermittent fracture propagation, is now approximated with scalar time-dependent value. It turns out to be a reasonable simplification for intermittent fracture growth, where each fracture event is followed by a pressure drop. A finite volume method is now used for the solving of fluid flow problem, which assures that the model is volume conservative. The volume injected through the well is then the same as the volume of the fracture plus the volume leaked-out through the fracture walls into the rock.

Another difference with the current model is that the condition for tensile fracture propagation is a critical fluid pressure. The critical fracture pressure is slightly larger than the least compressive stress (Zoback, 2010). There are different models for the critical fracture pressure, which are based on the surface energy of rupture. The surface energy is the energy needed to tear a unit area of the rock apart. Two models of critical fracture pressure are discussed. The use of critical fracture pressure is a simple and practical condition because the critical pressure can be taken from well tests. Furthermore, a condition on the fluid pressure does not require the calibration of a critical stress in the elements. The most stressed elements will fracture when the critical fluid pressure is exceeded. The numerical model solves for the stress and strain in the poro-elastic rock using the far-field stress as boundary conditions.

The elements can be assigned an individual random strength that allows for branching fractures in heterogeneous rocks. The stress enhancement at the fracture tips can be used for selecting the next element to break. The intermittent nature of fracturing is demonstrated, where the least increment in fracture length is the size of an element. Several elements at different places may break at one time step until no more elements are critically stressed.

The conditions for a critical fluid pressure allows for the derivations of simple analytical models for hydraulic fracturing of homogeneous low permeable or impermeable rocks. Conditions for tensile (mode I) fracture propagation are discussed in light of these models. The analytical models are also useful for validating the numerical code.

The initialization of the fracture process at the well is not a part of the modelling. Therefore, the model deals with the propagation on an initially small fracture, which in

the following examples has the size of three elements. These elements are the injection-element and its two neighbour elements.

The main features of the proposed numerical model of hydraulic fracturing is that it is based on a poroelastic rock, and that it has volume conservative intermittent fracture propagation without any special gridding. Volume conservation implies that the volume of fluid in the fracture plus the volume of fluid that has leak-off into the rock is equal to the fluid volume that has been injected. The use of a critical fracture pressure has the advantage that it can be related to the surface energy of fracturing or it can be taken as an input parameter from well tests. Non-linear fractures can be modelled using random rock strength.

The previous models of Wangen (2011, 2013) also compute the fracture volume, but it is not used directly in a volume balance. The fracture volume enters the pressure equation indirectly as fracture porosity in the fractured elements. The fracture porosity in an element is based on the fracture volume in the element, when it is evaluated at the previous time step. The volume balance for the models of Wangen (2011, 2013) is not thoroughly tested for a low permeable rock, where most of the injected fluid is in the fracture. The opposite case, for a permeable rock, has volume conservative properties as a standard finite element method, because the leaked-out volume is almost the same as the injected volume.

The advantage with the finite volume method, compared to the finite element method, with respect to mass and volume conservation is that the finite volume method gives directly the mass or volume flow across element interfaces. Every element is mass or volume conservative with respect to flow from the neighbour elements. Therefore, it is straightforward to compute the leak-off from the fracture using the finite volume method. A standard finite element method does not provide the flow at the interfaces of the elements, and it is therefore not suited for applications where mass or volume flow between elements are of interest.

This paper is organized as follows. The poro-elastic assumptions about the rock are reviewed. It is shown how the fracture is represented in the numerical model, before the condition for fracture propagation is explained. Simple exact models for fracture propagation in impermeable and homogeneous rock are presented, and an exact model

is used to verify the numerical code. Examples are given of hydraulic fracturing in the permeable and homogeneous rock, and then in low-permeable and heterogeneous rock.

2. Poro-elastic rock

The numerical model of hydraulic fracturing is based on Biot poro-elasticity for the rock. The equations for poro-elasticity are two coupled equations - one for the displacement field and another for the pore fluid pressure (Wang, 2000). The equation for the displacement field is obtained from mechanical equilibrium

$$\sigma_{ij,j} + g\,\delta_{i3} = 0 \tag{1}$$

where summation is assumed over every pair of equal indices (Einstein's summation convention). The Kronecker delta is $\delta_{ij} = 0$ for $i \neq j$ and $\delta_{ij} = 1$ for $i = j$. Therefore, gravity drops out because $i = 1, 2$ for 2D models in the horizontal plane. In poro-elasticity the normal components of the stress field are modified by the fluid pressure

$$\sigma_{ij} = 2G\varepsilon_{ij} + \lambda\varepsilon_{kk}\delta_{ij} - \alpha p_f \delta_{ij} \tag{2}$$

where we have used the convention that compressive stress is negative. The shear modulus is $G = E/2(1+\nu)$ and $\lambda = E\nu/(1+\nu)(1-2\nu)$ is the Lamé-parameter, where E is Young's modulus, ν is the Poisson ratio, α is the Biot coefficient and p_f is the fluid pressure. The strain is given by the displacement field u_i as

$$\varepsilon_{ij} = \frac{1}{2}\left(\frac{\partial u_i}{\partial x_j} + \frac{\partial u_j}{\partial x_i}\right) \tag{3}$$

The pressure equation for the pore fluid is

$$\frac{1}{M}\frac{\partial p}{\partial t} - \nabla \cdot \left(\frac{k}{\mu}\nabla p\right) = -\alpha \frac{\partial \varepsilon_v}{\partial t} \tag{4}$$

where k is the permeability, μ is the viscosity, $\varepsilon_v = \varepsilon_{11} + \varepsilon_{22}$ is the volume strain and M is the system compressibility

$$\frac{1}{M} = \phi c_f + \frac{\alpha - \phi}{K_s} \tag{5}$$

where c_f is the fluid compressibility, ϕ is the porosity and K_s is solid grain modulus (Wang, 2000; Kim et al., 2011a). The pressure equation (4) is expressed in over-pressure $p = p_f - p_h$, which is the fluid pressure p_f minus the hydrostatic pressure p_h.

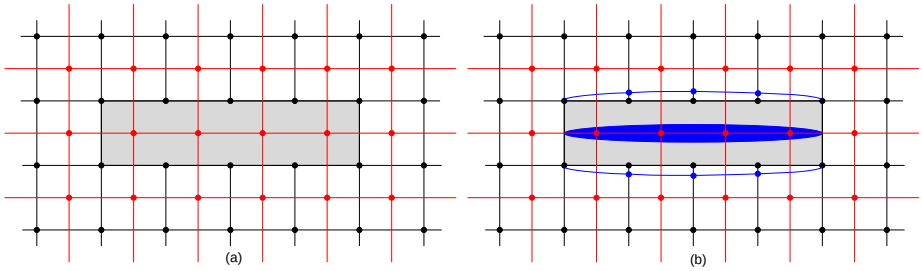

Figure 1: (a) The displacement equations are solved on the finite element grid (black) and the pressure equation is solved on the finite volume grid (red), which connects the element centers. (b) The blue nodes show the displacement of the nodes of an open fracture. The blue colored area in the center shows how the width of the fracture follows from the displacement field.

The initial fluid pressure is hydrostatic and the hydrostatic pressure remains constant in space and time. The changing fluid pressure is the cause for the deformations in the rock, since the boundary conditions are kept constant in time. The rock deformations have a feedback on the pressure equation though the rate of change of volume strain $\partial\varepsilon_v/\partial t$. These equations are solved numerically with a finite element method for the displacement equations and the finite volume method for the pressure equation. The so-called fixed-stress split is applied, which assures that a sequential solution of the two equations is unconditionally stable (Kim et al., 2011a,b).

A common approach to geo-mechanical modelling is to separate the stress field into two parts – where the first part is the initial stress field and the second part is the poro-elastic change to the initial stress field caused by fluid injection (Kim et al., 2011a; Alpak and Wheeler, 2012; Wangen, 2013). The current approach takes into account the full stress field. The computational domain is rectangular and the sides are oriented normal to the principal stresses. The initial stress field is normally anisotropic, and the principal stresses are therefore not the same.

The poro-elastic model remains linear in stress and fluid pressure as long as material properties are unchanged. On the other hand, hydraulic fracturing implies that the grid elements change properties as they fracture. The model is therefore not linear after breaking of elements.

3. Numerical model of the fracture

The fracture is represented on a regular grid as shown in figure 1. The elements in the grid are of two types – rock or fracture. The elements that constitute the fracture are different from the rock element by the Young's modulus, which are set very low in the fracture. Therefore, there is almost no elastic resistance in the fractured elements against opening. The fracture width is obtained from the nodes at the boundaries between the fracture and the rock, see figure 1. Figure 1 shows how the width is given as the difference between the displacements of the nodes situated across the fracture. The width obtained from a fractured element gives the fracture volume of the element, when it is multiplied with the element length and height. The height is taken to be $h = 1$ m in 2D. An alternative to the suggested approach, which is also based on a regular grid, is to represent the fracture by splitted nodes (Ji and Sullivan, 2009; Kim and Moridis, 2013, 2015). Then, the fracture follows a chain of nodes rather than a chain of elements. The node-splitting technique is simple to apply when the fracture is assumed symmetrical and only one side of it is represented by the numerical grid. The fracture surface can then be represented by free surface nodes of the grid (Ji and Sullivan, 2009). Node splitting becomes less straightforward to implement for fractures that cannot be represented by surface nodes of the grid, for instance a branching fracture inside the grid.

The finite volume method allows for a volume conservative formulation of the fracture by requiring that the volume increment of fluid (dV_{in}) that is injected during a time step is equal to the volume increment of fluid in the fracture (dV_{fr}) plus the volume increment of fluid that leaks out through the fracture walls (dV_{lk})

$$dV_{\mathrm{in}} = dV_{\mathrm{fr}}(p_{\mathrm{fr}}) + dV_{\mathrm{lk}}(p_{\mathrm{fr}}) \tag{6}$$

The fluid pressure is taken to be a scalar value p_{fr}. The fracture volume increment and leak-off volume increment are then dependent on just one value, the fracture fluid pressure p_{fr}. This is a simplified description of fluid flow in a fracture with intermittent propagation, which assumes that the fracture conductivity is sufficiently good for the pressure gradients within the fracture to be small.

It was early recognized that most of the pressure drop inside a fracture is towards the tips, where the width goes to zero (Khristianovic and Zheltov, 1955). Numerical simulations also demonstrate that the pressure inside the fracture is almost the same as the injection pressure because of its high permeability (Kim and Moridis, 2013). It is straightforward to estimate the pressure gradient and the pressure drop along a fracture, assuming laminar flow and a parallel plate fracture permeability. From Darcy's law the pressure gradient becomes

$$q = wh\frac{w^2}{12\mu}\frac{dp}{dx} \qquad \text{or} \qquad \frac{dp}{dx} = \frac{12\mu q}{hw^3} \tag{7}$$

where q is the injection rate given as volume per time and where wh is the cross section of the fracture. Using $w = 3$ mm, $h = 1$ m, $\mu = 1 \cdot 10^{-3}$ Pa s, $q = V/t$, where $V = 50$ m^{3}and $t = 1$ day gives a pressure drop $dp = (dp/dx)\ a = 0.03$ MPa over a distance $a = 100$ m. If there is leak-off in the fracture then the rate q decreases towards the tips and the estimation for the pressure drop dp becomes even less.

This model has intermittent fracture growth, and the fracture propagates with at least the length of an element at each discrete event. The instantaneous propagation of the fracture leads to transients in the fluid pressure. The duration of a transient can be estimated by the half-life for a transient in a system with constant parallel plate permeability along the fracture. An estimate for the half-life is

$$t_{1/2} = \frac{\ln 2\, c_f l^2\, \mu}{\pi^2 k_f} \tag{8}$$

where c_f is the fluid compressibility, l is the full length of the fracture, μ is the viscosity and $k_f = w^2/12$ is the parallel plate permeability when the fracture width is w (Wangen, 2010). An order of magnitude estimate with $c_f = 5 \cdot 10^{-10}$ Pa, $l = 1000$ m, $\mu = 1 \cdot 10^{-3}$ Pa s and $w = 1$ mm gives that $t_{1/2} = 0.4$ s. This estimate can be considered an upper bound on the time constant since a fracture normally has less length and larger width.

The volume balance (6) for the fracture pressure p_{fr} is solved by use of a Newton-Raphson scheme at each time step. The Newton-function is the mismatch in the volume balance (6), which is the scalar function $f(p_{\text{fr}}) = dV_{\text{fr}}(p_{\text{fr}}) + dV_{\text{lk}}(p_{\text{fr}}) - dV_{\text{in}}$ as a function of p_{fr}. The function $f(p_{\text{fr}})$ is computed by the following steps.

1. The fluid pressure is obtained by solving the pressure equation (4) with the finite volume method, with the fracture pressure p_{fr} used as a Dirichlet boundary condition in the fractured elements. The external boundaries of the grid has zero overpressure as a Dirichlet boundary condition.
2. The displacement field, which is generated by the fluid pressure from step 1, is found by solving the equilibrium equations (1) using the poroelastic stress-strain relationship (2) and the definition of strain (3). The numerical solution uses a standard finite element method with bilinear basis functions.
3. The increment dV_{fr} is the difference between the current fracture volume and the fracture volume at the previous time step. The fracture volume is computed as the difference in area of the deformed element and the initial undeformed element. The nodes positions of the deformed element are the displacement of the nodes added to the initial nodes positions.
4. The volume increment of leaked off fluid dV_{lk} is computed by adding the volume flux, multiplied with the current time step, in all transmissibilities that connect the fractured elements with the intact rock elements.
5. The increment in injected volume is $dV_{\mathrm{in}} = q\Delta t$, where q is the injection rate and Δt is the current time step.
6. The mismatch in the volume balance for fracture pressure p_{fr} is then computed as $f = dV_{\mathrm{fr}} + dV_{\mathrm{lk}} - dV_{\mathrm{in}}$.

The derivative of the Newton-function $f(p_{\mathrm{fr}})$ is computed numerically. The convergence of the scheme is fast because the increments of fracture volume and the leak-off volume depend nearly linearly on the fracture pressure p_{fr}. The fracture pressure from the previous time step is taken as the initial value for the Newton-Raphson scheme.

The mechanics problem is solved with a standard finite element approach using bilinear basis functions, where the unknowns are obtained at the nodes of the grid. The fluid flow problem is solved with basis functions that are constant on the elements, and where the unknowns are found at the center of the elements. This is a mixed finite element approach with a common choice of basis functions. The weak formulation of the fluid flow problem gives a finite volume method, where the element centers are

connected by transmissibilities (Kim et al., 2011a).

4. Fracture propagation

The fracture fluid pressure in an impermeable rock needs to exceed the least compressive stress in order to open (Zoback, 2010). In addition, rock strength gives how far the fracture can open before it breaks and propagates. Then, in case of a homogeneous rock the fracturing process creates a planar fracture normal to the least compressive stress, because of the stress enhancement at the fracture tips. The strength can be converted to a critical fracture pressure in case of a linear fracture in a homogeneous and impermeable rock. A linear fracture, as a slit in an infinite material, has the critical pressure

$$p_c(a) = \sigma_h \cdot \Big(1 + \frac{2a_0}{a}\Big)^{1/2} \quad \text{where} \quad a_0 = \frac{\gamma E'}{\pi \sigma_h^2} \tag{9}$$

for surface energy of rupture γ, least compressive stress σ_h and half-length a, as shown in Appendix A. The modulus E' is $E' = E$ for plain stress conditions and $E' = E/(1-\nu^2)$ for plain strain conditions, where E is the Young's modulus (Jaeger et al., 2007). It is practical to express p_c with the characteristic length a_0, because $p_c(a)$ behaves differently in the two regimes $a \ll a_0$ and $a \gg a_0$. It has been common to express the critical fracture pressure as (Perkins and Kern, 1961; Mack and Warpinski, 2000)

$$p_c(a) = \sigma_h + \Big(\frac{2a_0}{a}\Big)^{1/2} \tag{10}$$

which simplifies the derivation of analytical models for the hydraulic fracturing compared with (9). The difference between the critical fluid fractures (9) and (10) is that the latter do not account for the fact that the fracture is closed for $p_f < \sigma_h$ (see Appendix A). The fracture toughness can be obtained from the surface energy of rupture for tensile fracture as $K_I = (2\gamma E)^{1/2}$, (Jaeger et al., 2007). The surface energy, the fracture toughness and the Young's modulus are rock properties.

Well testing shows that fracture propagation takes place for well pressure that is a flat plateau (Zoback, 2010). The critical pressure (9) starts out as a high pressure close to the well and then it decreases towards a plateau, which is the least compressive stress. A problem with the critical fracture pressure (9), is that it becomes almost the

same as the least compressive stress for $a \gg a_0$. The regime $a \gg a_0$ is outside the near-well area for reasonable values of the least compressive stress and surface energy. Therefore, the fracture is almost closed outside the near-well region where $a \gg a_0$. An almost closed fracture implies that the fracture must propagate very far in a tight rock in order to have a volume that is large enough to hold the fluid that is being injected.

The critical fracture pressure is approximated by a constant well pressure, which becomes an input parameter. It is very convenient to have a condition on the fluid pressure, because it can be compared directly with the fracture propagation pressure measured by well testing. The hydraulic fracture process is driven by the difference between the critical pressure and the least compressive stress. This difference is now given as input, rather than having it estimated from rock strength and permeability.

Even though the fracture condition is in terms of a critical fluid pressure we need a criterion for selecting elements along the fracture surface to break. The straightforward approach is to select the most stressed (or strained) elements. These are found at the two tips of the fracture in a 2D rock with homogeneous properties. In case of symmetrical propagation all equally and maximally stressed (or strained) elements will fracture when the critical fluid pressure is exceeded. The breaking of elements implies that they have their Young's modulus changed to a low value, which assures that they give very little elastic resistance to fracture opening. The full pressure- and stress fields are recomputed after each breaking event. The numerical algorithm will continue to break maximally stretched elements until the fluid pressure is brought below the critical fluid pressure. It is also possible to combine the critical fluid pressure with a random element strength. The element to break will then be the most stressed element relative to a random strength level.

The volume of fluid in the fracture is assumed to be the same right after a fracture event as it was right before, and less fracture width is needed for a long fracture to give the same fracture volume as a short one. Therefore, fracture events lead to less fracture width and a pressure drop in the fracture. For an elliptical fracture in an impermeable rock the pressure drop becomes

$$p_2 - \sigma_h = \left(\frac{a_1}{a_2}\right)^2 \Big(p_1 - \sigma_h\Big) \tag{11}$$

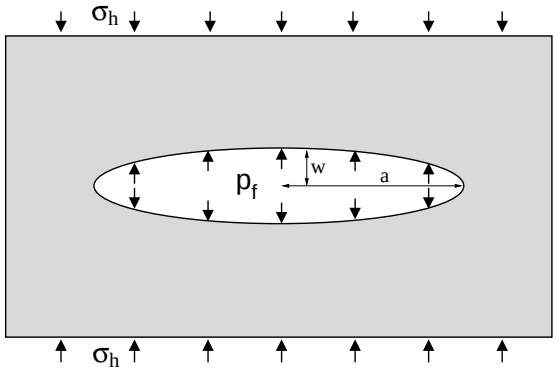

Figure 2: A slit in a 2D rock becomes an elliptical fracture when it is loaded from the inside with a fluid pressure p_f and with a remote stress field σ_h normal to the fracture.

where p_1 and p_2 are the pressures at fracture half-lengths a_1 and a_2, respectively. The pressure drop (11) follows from the expression for the volume of an elliptical fracture (14). Pressure drop after a fracture event is observed in models with intermittent fracture propagation (Tzschichholz and Wangen, 1998; Kim and Moridis, 2015).

5. Exact models for hydraulic fracturing of impermeable rock

5.1. Constant critical pressure

Simple and exact models for hydraulic fracturing are reviewed in this section, which applies for the special case of an impermeable and homogeneous rock. The model is based on the solution for the displacement field of a slit in an infinite 2D plate subjected to a constant remote stress field, and where the walls of the slit is loaded with a constant fluid pressure. The slit becomes an elliptical fracture with the half-width (see figure 2)

$$u(a, p_f, x) = \frac{2}{E'} (p_f - \sigma_h)\big(a^2 - x^2\big)^{1/2} \tag{12}$$

where x is a position along the fracture (Jaeger et al., 2007). The fluid pressure is constant in the fracture, and the fracture is oriented normal to the minimum principal stress (Zoback, 2010). The solution shows that the fluid pressure must exceed the remote stress field, $p_f > \sigma_h$, for the fracture to open. The opening is at maximum at the center of the fracture (the injection point at $x = 0$) where the half-width is

$$u_{\max}(a, p_f) = \frac{2}{E'} (p_f - \sigma_h)a \tag{13}$$

Property	p_c constant	$p_c(a)$ for $a \ll a_0$	$p_c(a)$ for $a \gg a_0$
$p_c(t)$	const	$2\gamma^{2/3}\left(\frac{E'}{\pi qt}\right)$	$\sigma_h + \frac{\gamma^2 E'}{\pi\sigma_h^2 qt}$
$a_c(t)$	$\left(\frac{E'qt}{2\pi(p_c-\sigma_h)}\right)^{1/2}$	$\frac{1}{2}\left(\frac{E'}{\pi\gamma}\right)^{1/3}(qt)^{2/3}$	$\frac{\sigma_h qt}{2\gamma}$
$u_{\max,c}(t)$	$\left(\frac{2\pi(p_c-\sigma_h)qt}{\pi E'}\right)^{1/2}$	$2\left(\frac{1}{\pi}\right)^{2/3}\left(\frac{\gamma qt}{E'}\right)^{1/3}$	$\frac{2\gamma}{\pi\sigma_h}$

Table 1: The three columns show critical fracture fluid pressure $p_c(t)$, critical fracture length $a_c(t)$ and max critical fracture half-width $u_{\max,c}(t)$ as a function of time for three analytical models for fracturing of impermeable and homogeneous rock. The three models are: (1) constant critical fracture fluid pressure, (2) critical fluid pressure $p_c(a)$ given in the regime $a \ll a_0$, (3) critical fluid pressure $p_c(a)$ given in the regime $a \gg a_0$.

and the volume of the elliptical shaped fracture becomes

$$V(a, p_f) = \pi a \cdot u_{\max}(a, p_f) = \frac{2\pi(p_f - \sigma_h)a^2\, h}{E'} \tag{14}$$

where h is vertical height of the fracture. A unit height $h = 1$ m is used in the following. The critical fracture volume V_c is obtained by setting the fluid pressure equal to its critical value p_c = const. The injected volume is $V = q\,t$ for a constant volume injection rate q. Solving $V_c = qt$ for a gives the critical fracture half-length as a function of time

$$a_c(t) = \Big(\frac{E'qt}{2\pi(p_c - \sigma_h)}\Big)^{1/2} \tag{15}$$

The critical pressure and the critical half-length a_c can then be inserted into maximum fracture width (13), which gives the critical fracture width

$$u_{\max,c}(t) = \Big(\frac{2(p_c - \sigma_h)qt}{\pi E'}\Big)^{1/2} \tag{16}$$

The constant critical fracture pressure leads to a critical fracture length and critical maximum half-opening that both increase as $\sim \sqrt{t}$. One way to check these expressions is to verify that the fracture volume is $V_f = \pi u_{\max,c}(t)\, a_c(t) = qt$. The critical half-length (15), the critical half-width (16) and the critical volume $V_c = qt$ are used to verify the numerical model, when the critical pressure is p_c = const.

5.2. Critical pressure by surface energy

The critical pressure (9), which takes into account the surface energy of rupture, can be used as a basis for the derivation of alternative expressions for the critical properties: the half-length $a_c(t)$ and the maximum half-width $u_{\mathrm{max,c}}(t)$. The critical pressure (9) is derived in Appendix A. It is not straightforward to derive simple expressions for $a_c(t)$ and $u_{\mathrm{max,c}}(t)$ directly from the critical pressure (9). On the other hand, this task is considerably simplified when it is done separately for the two different regimes of critical pressure, as defined by the half-lengths $a \ll a_0$ and $a \gg a_0$, as shown in Appendix A.

The regime $a \ll a_0$, which applies for shallow depths (small values for σ_h) or short fractures, has a critical fracture length and a critical half-width that go as $\sim t^{2/3}$ and $\sim t^{1/3}$, respectively. This is similar to the model of Perkins and Kern in the case of no leak-off (Mack and Warpinski, 2000), although their expressions do not involve surface energy of fracturing.

The other regime $a \gg a_0$, which is the one relevant for layers under compressive stress, have a critical half-length that increases linearly with time. Therefore, the critical maximum half-width is constant as a function of time. A constant critical maximum fracture width as a function of time does probably not give a good description of a dynamical fracture shape. The critical half-opening is also very small. For example, a surface energy $\gamma = 100$ J m^{-2} and a least compressive stress $\sigma_h = 10$ MPa gives a maximum fracture opening $\sim 10^{-5}$ m. Such a small width is also consistent with the corresponding critical fracture pressure that is just slightly higher than the least compressive stress. The critical properties of the different models are collected in table 1.

6. Verification of the model

The exact model, based on constant critical pressure, is well suited for verification of the numerical model, for the special case of an impermeable and homogeneous rock. The fracture opens when the fluid pressure exceeds the least horizontal stress $\sigma_h = 10$ MPa and it propagates when it exceeds the constant critical pressure $p_c = 11$ MPa. The least compressive stress could be typical of a depth range from of 1 km to 2 km,

depending on the geological setting. The other parameters in the model are a Young's modulus $E = 10$ GPa, a maximum horizontal stress $\sigma_H = 15$ MPa, a Poisson ratio $\nu = 0.25$, an injection rate $q = 50$ m^3 day^{-1} and a grid size $\Delta a = 10.05$ m. The full set of parameters for this model is found in the column "Imperm" in table 2.

Figure 3a shows the numerically computed fluid pressure in the center of the fracture. A fracture event is triggered when the numerical fluid pressure exceeds the critical pressure, which is shown as the straight line. The fluid pressure exceeds the critical pressure because the timestepping steps beyond the time of fracturing. The exact time step of fracturing is not estimated. The instantaneous propagation of the fracture leads to a pressure drop. The volume of the fluid in the fracture remains the same right after the event as it was right before the event. But a longer fracture needs less fracture width, and therefore less fluid pressure in order to have the same volume. The first pressure drops are largest because the relative elongation of the fracture is largest for the first events. The fracture is initially 3 elements long, and the first event extends it from 3 to 5 elements. The initiation of the fracture from the bore hole is not a part of the modelling. After the instantaneous drop, the fluid pressure continues to increase because of constant injection. A new fracture event is once more triggered when the fluid pressure exceeds the critical value. The fracturing process limits the fluid pressure to the critical pressure as seen from figure 3a.

Fracturing in the numerical code makes the most stressed elements change properties from rock to fracture, and it continues to fracture elements until the fluid pressure is below the critical pressure. The most stressed elements are found at the two tips of a linear fracture that propagates symmetrically away from the injection element.

Figure 3b shows the discrete fracture growth of the numerical model. The fracture has the same length until an event is triggered, and then the fracture half-length extends with $\Delta a = 10.05$ m. Therefore, the fracture length produced by the numerical model appears as a staircase. The smooth critical fracture length of the exact model is also shown, and the staircase follows the critical fracture length.

The volume of the fracture, computed by the numerical model, is shown in figure 3c. The volume matches very closely the injected volume. This is as expected, because the fluid pressure in the fracture is at all times computed in order to match the

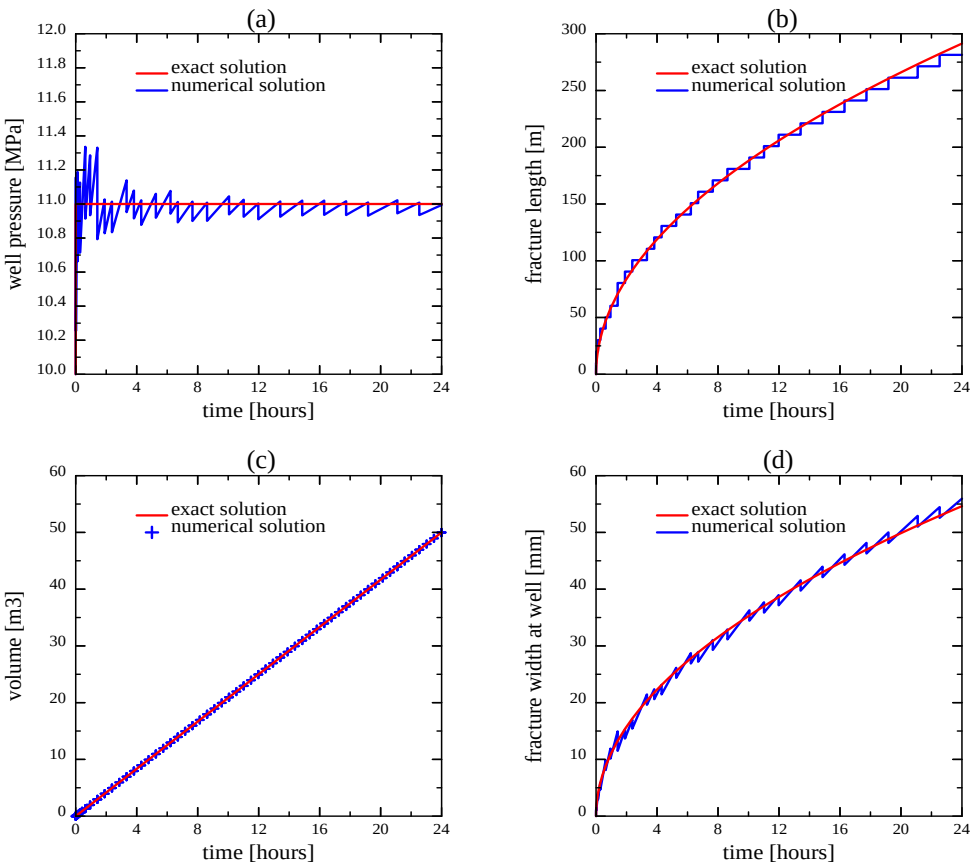

Figure 3: (a) The critical fracture fluid pressure as a function of time. (b) The critical fracture length as a function of time. (c) The critical fracture volume as a function of time. (d) The critical fracture half-opening at the well as a function of time.

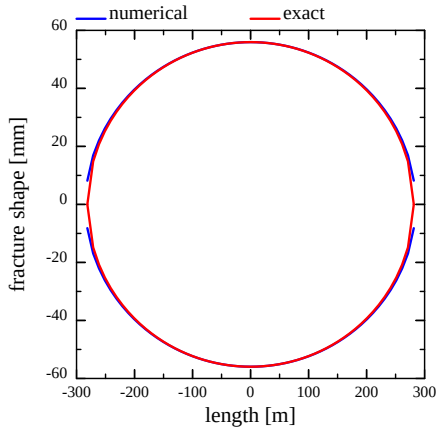

Figure 4: The displacement field of nodes surrounding the upper half of the fracture is compared with the exact displacement of equation (12). See the text for details.

injected volume, as expressed by equation (6). For an impermeable rock this relation becomes $V_{\mathrm{fr}}(p_f) = V_{\mathrm{in}}$.

The maximum half-opening $u_{\max}$, which is for the injection element, is plotted in the figure 3d. The half-width makes an instant drop each time there is a fracture event, otherwise it increases as a result of pressure build-up from fluid injection at a constant rate. The match against analytical model for continuous fracture growth is good.

The ability of the numerical model to reproduce the exact results depends on its ability to produce an elliptical fracture at a constant fluid pressure. Figure 4 shows the numerically computed fracture shape at the end of the simulation at $t = 24$ h, and that it compares well with the exact shape given by equation (12).

7. Hydraulic fracturing of permeable rock

A permeable case is different from the impermeable by the leak-off of fluid through the fracture walls. The volume balance for the fracture is now given by equation (6). It says that an injected volume increment is equal to a volume increment of the fracture plus a volume increment of fluid lost through the fracture walls. The case has a rock

Parameter	Imperm	Perm	Rand	Units
number of nodes x-dir	200	100	300	-
number of nodes y-dir	200	100	300	-
grid length (x- and y-dir)	2000	2000	2000	m
porosity (ϕ)	0.15	0.15	0.15	-
permeability (k)	0	1e-15	1e-18	m^2
Poisson ratio (ν)	0.25	0.25	0.25	-
Biot coefficient (α)	1	1	1	-
Young's modulus (E)	1e+10	1e+10	1e+10	Pa
fluid compressibility (c_f)	5e-10	5e-10	5e-10	Pa^{-1}
fluid density (ϱ_f)	1000	1000	1000	$\mathrm{kg\,m}^{-3}$
fluid viscosity (μ)	0	0.001	0.001	Pa s
fluid fracture pressure (p_c)	1.1e+07	1.1e+07	1.1e+07	Pa
min horizontal stress (σ_h)	-1e+07	-1e+07	-1e+07	Pa
max horizontal stress (σ_H)	-1.5e+7	-1.5e+07	-1.5e+07	Pa
injected volume (V_{in})	50	50	50	m^3
time span	86400	86400	86400	s

Table 2: The parameters used in the three different cases.

permeability $k = 1 \cdot 10^{-15}$ m^2, a Young's modulus $E = 10$ GPa and a Poisson ratio $\nu = 0.25$. A volume of $V_{\mathrm{in}} = 50$ m^3 is injected during a time span of 24 h. The parameters in this case study are found in the table 2 in the column named "Perm".

The pressure at the injection point is shown in figure 5a. It rises until it exceeds the critical pressure $p_c = 11$ MPa, and a fracture event is triggered. The fracture event is followed by a pressure drop, because a longer fracture needs less fracture width, and therefore less pressure, to make volume for the same fracture fluid. The numerical pressure over-shoots the critical pressure for the first events, because the numerical model does not try to estimate the exact time of rupture. Initially, there is a steep pressure increase with time, which becomes less and less steep as the fracture grows. The time steps are marked with dots on the curve that shows the numerical fluid pressure. The intermittent fracture growth is shown in figure 5b by the fracture half-length as a function of time. Each event is the rupture of the two tip elements, and the half-length grows instantaneously with the length of one element ($\Delta a = 20.2$ m). The fracture has initially the half-length the size of one element ($\Delta a = 20.2$ m), since fracture initiation from the well is not a part of the modelling.

The stress field σ_{yy} at $t = 24h$ h is shown in figure 6a, and the stress concentration

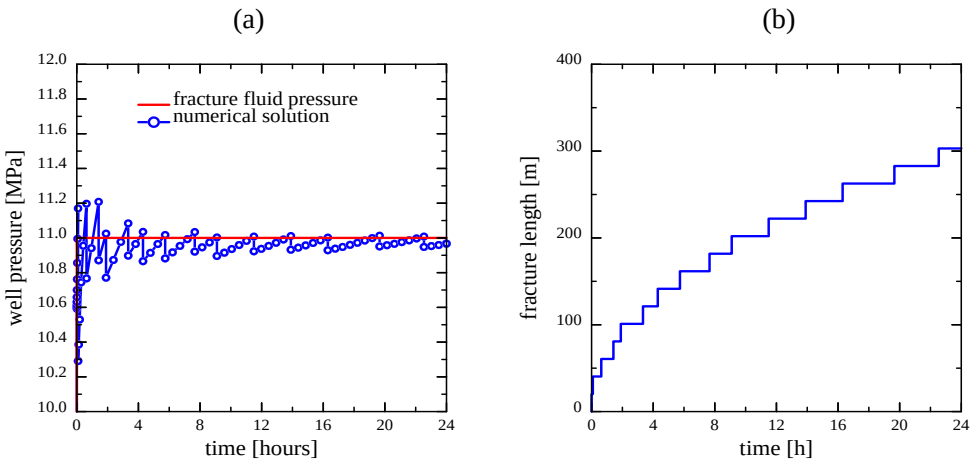

Figure 5: (a) The well pressure during hydraulic fracturing of a permeable rock. (b) The fracture length as a function of the time corresponding to the well pressure shown in (a).

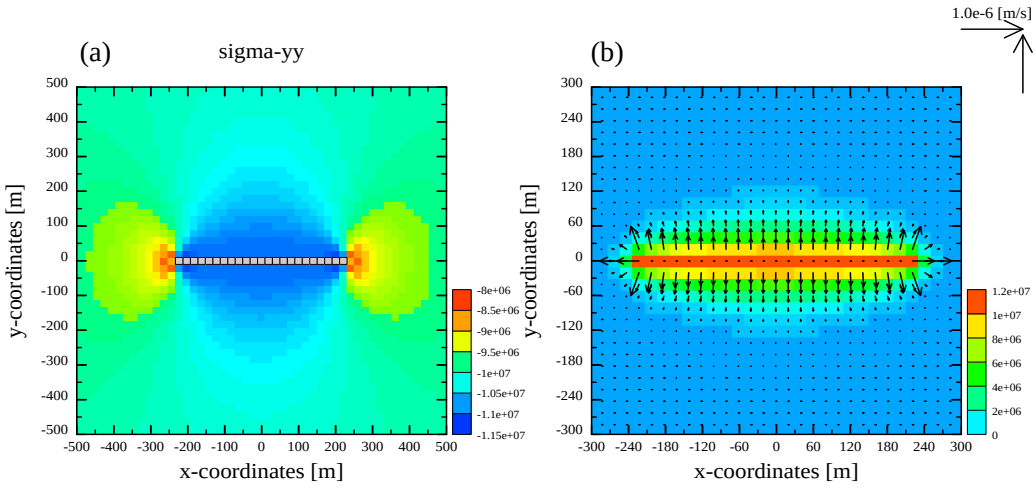

Figure 6: (a) The effective stress at time $t = 24$ h. (b) The overpressure and the Darcy flux at $t = 24$ h.

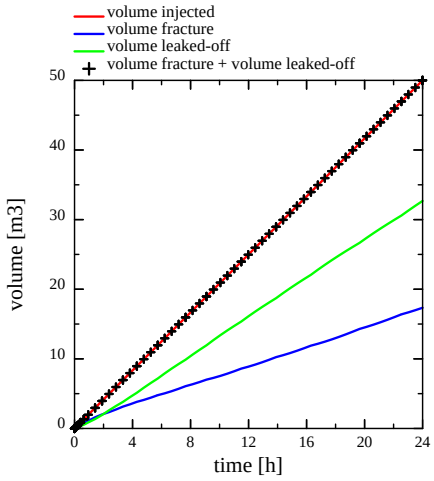

Figure 7: Fluid volumes as a function of time during the hydraulic fracturing process.

around the fracture tips are clearly seen. Therefore, these are the elements that break during fracture growth, since the rock strength is homogeneous. The stress enhancement is grid size dependent, and it increases with decreasing grid size. The increase in the tip stress of a linear fracture scales as $\sim r^{-1/2}$ for a constant fracture fluid pressure, where r is the element size (Wangen, 2011, 2013). This is the same behaviour as for the tips of an ideal linear fracture (Lawn, 1993). The current grid size is not sufficiently small for the stress state at the center of the elements at the fracture tips to go from a compressive state to a tensile state. The advantage of using a critical fracture pressure, on a grid with equally sized elements, is that the grid size is less important. What is important is that the most stressed element (or elements) is identified and broken when the critical fracture pressure is exceeded.

The fluid pressure and the Darcy flow field at $t = 24$ h are shown in figure 6b. The Darcy flow vectors are longest at the fracture tips, where the pressure gradient in the rock is largest. The pressure gradients are less outside the center part of the fracture, where the leak-off has lasted longest.

The fluid volume balance during injection is shown in figure 7. Both fluid leak-off and accumulation of fluid in the fracture take place from the start. The fracture is

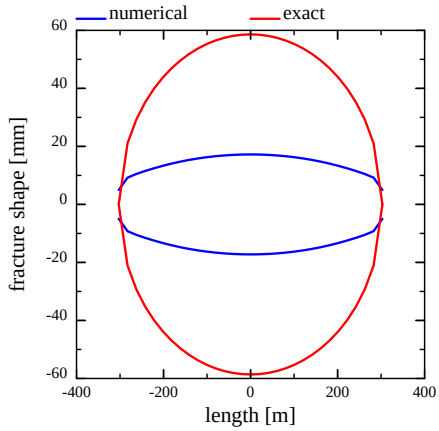

Figure 8: The numerical fracture has less width than an equally long fracture in an impermeable rock inflated with the same fluid pressure.

propagating rapidly at the start and the volume accumulation in the fracture is slightly larger than the leak-off. At the time $t = 2$ h there is roughly equal amounts of fluid in the fracture as that has leaked-out, and the volume of leak-off dominates after $t = 2$. The fluid volume in the fracture increases smoothly, even though the fracture growth is intermittent with pressure oscillations. The sum of the fracture volume and leak-off volume is also shown in figure 7, which is exactly matching the injected volume. Therefore, the volume balance (6) is very good at all times.

The shape of the fracture after 24 h of injection is shown in figure 8. It is compared with an equally long fracture in an impermeable rock with the same fluid pressure. The width is less in the case of leak-off, because leak-off makes the fluid pressure dissipate into the host rock around the fracture.

8. Hydraulic fracturing of heterogeneous rock

The fracturing procedure looks for an element to break when the fluid pressure exceeds the critical pressure. Instead of looking for the least compressed (most tensile) element, the procedure could look for the least compressed element relative to a random

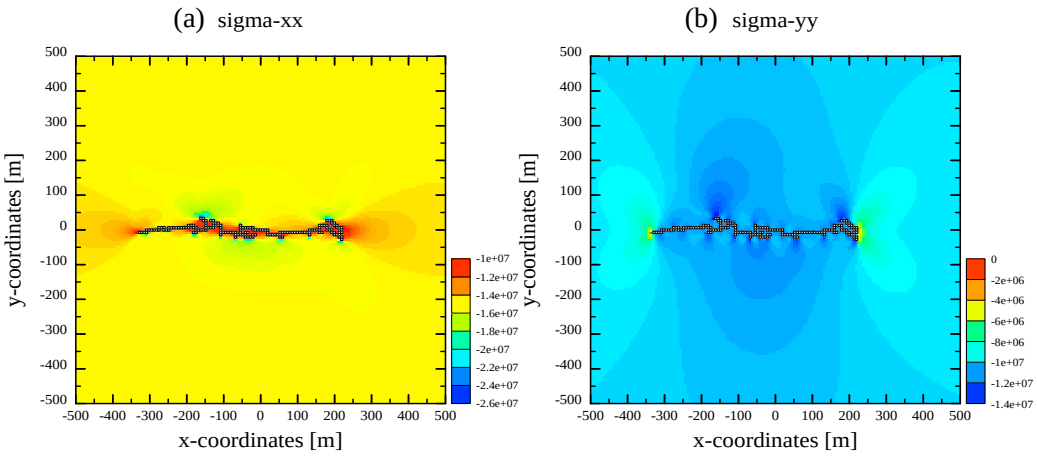

Figure 9: The stress around the fracture at time 24 h. (a) The stress σ_{xx} and (b) the stress σ_{yy}.

strength level. Each element can be assigned an individual random strength, which makes some elements weak and other strong. The element with the largest difference between the computed stress and its random stress level is selected as the element to break, when the fracture fluid pressure exceeds the critical pressure. The random strength level allows for a simple way of selecting an element to break, where the section is controlled by both the computed stress and a random element strength. Any element along the fracture surface is then possible candidates for breaking, not just the two stressed tip elements, where the tensile stress enhancement is strongest. This allows for a non-linear fracture growth and a branching fracture.

Figure 9 shows an example of fracture growth with random element strength. The strength is obtained by multiplying the average strength $\sigma_m = -2.5 \cdot 10^7$ Pa with a random number r. (Negative stress is compression.) The random numbers r are produced with the normalized distribution $r(\rho) = (n+1)\,\rho^n$ with $n = 1/2$, and where ρ is uniformly distributed.

The maximum compressive stress is $\sigma_H = -15$ MPa in the x-direction and least compressive stress is $\sigma_h = -10$ MPa in the y-direction. The compressive stress along the fracture becomes reduced, but the tips of the side branches become compressed

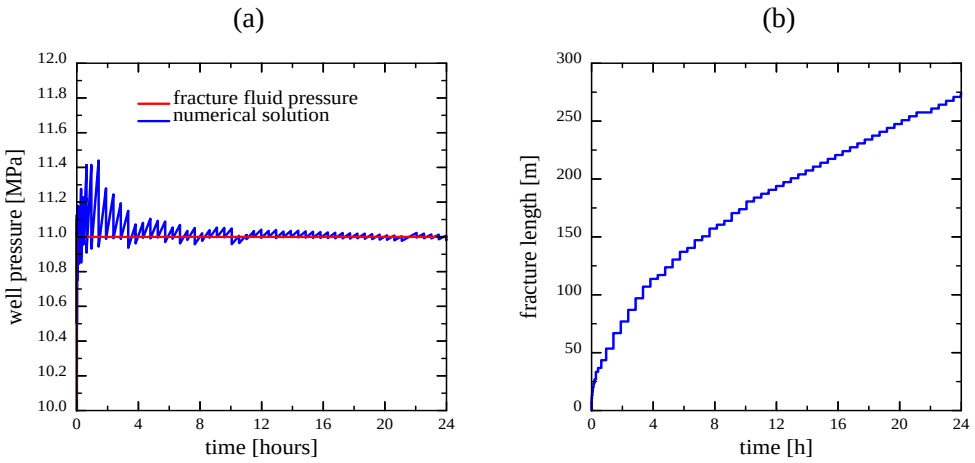

Figure 10: (a) The well pressure during hydraulic fracturing of a low permeable and heterogeneous rock. (b) The fracture length as a function of the time corresponding to the well pressure shown in (a).

in the x-direction. The stress field in the y-direction (σ_{yy}) shows the strongest tensile stress enhancement at the most distant fracture tips, and much less stress concentration at the tip of the branches along the fracture. The σ_{yy}-stress also shows that the sides of the fractures become compressed due to the fracture opening.

An analysis of the element breakage during the injection process showed that extending the fracture laterally by breaking a distant element reduced the fluid pressure more than breaking an element on a side branch close to the center. The fluctuations in the fluid pressure during the injection operation is shown in figure 10a. The fluid pressure is close to the fracture pressure after the first phase of fracture growth. The fracture is mainly growing in the x-direction, even though the elements have random strength. Stronger randomness can be assigned to the elements, and increasing the randomness makes the stress computation less important for fracture propagation.

The volume balance in figure 11 shows that there is very little fluid leak-off compared to what is stored in the fracture. The reason is the low permeability $k = 10^{-18}$ m^2.

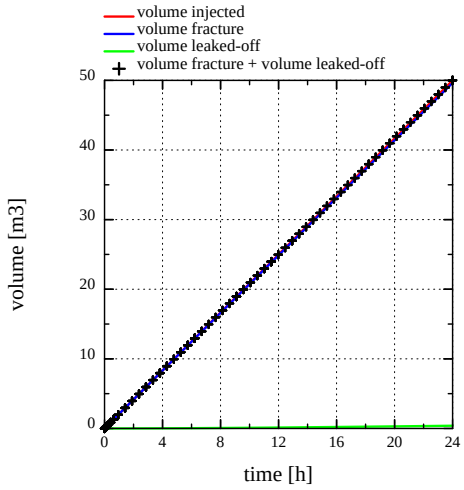

Figure 11: Nearly all the injected fluid fills the fracture, and almost nothing leaks out during time span of 24 h.

9. Conclusion

A volume conservative numerical framework is suggested for modelling of hydraulic fracturing in 2D – the injected volume is at all times equal to the volume that has leaked out and the volume of fluid that has accumulated in the fracture. The model is based on Biot's poro-elasticity for the rock. The numerical model makes use of a regular finite element grid on a reservoir scale, without any special gridding of the fracture. Boundary conditions are the far-field maximum and minimum principal stresses for the x- and y-directions, respectively. The mechanics problem is solved with the finite element method, and the fluid flow problem is solved with a finite volume method, which provides volume conservation for the fracture. The fluid flow in the fracture is approximated by a time-dependent scalar fluid pressure. The fracture propagates by discrete events followed by a pressure drop. The duration of a pressure transient following a fracture event is estimated, and it is found to be less than a second for a mm-wide fracture. Intermittent fracture propagation is modelled with a critical fluid pressure alone or in combination with elements that are assigned strength in terms of stress (or strain) limits. The numerical implementation is validated against an analytical model for an

impermeable and homogeneous rock, where the critical fluid pressure is constant. A non-constant critical fluid pressure is also derived on the basis of fracture surface energy. But this critical pressure is found less useful than a constant critical pressure, which can be taken directly from well tests. The numerical framework for hydraulic fracturing is applied on a permeable rock, which demonstrates volume conservation. The model is easily adapted to heterogeneous rocks by assigning random strength to the elements, and an example is given that shows the development of a branching fracture. The fracturing of low permeable rocks shows that most of the injected fluid remains in the fracture when the operation stops, and that little fluid leaks out into the host rock.

10. Acknowledgement

Parts of this work have been supported by the Research Councile of Norway through the projects 233736/E20 “Protect” and 244570/E30 “StressLess”. The author is greatful for the comments and corrections made be three anonymous referees.

11. Appendix: The critical fracture pressure for a linear fracture in a homogeneous and impermeable rock

Equation (12) gives the displacement field normal to an impermeable fracture wall. The incremental work done on the fracture wall by increasing the fluid pressure by dp is therefore

$$dW = 2 \cdot \Big(p\, h\, dx\Big)\Big(\frac{2}{E'}\sqrt{a^2 - x^2}\, dp\Big) \tag{17}$$

where the first parenthesis is the force over the wall area $h\, dx$ and the second parenthesis is the distance the wall element is displaced. The factor 2 represents the two fracture walls of a linear fracture. The work done by inflating the fracture to a pressure p is obtained by integrating over the fluid pressure from σ_h to p and over x from $-a$ to a. The fracture is assumed closed for pressures that are lower than σ_h. The work becomes

$$W(a,p) = \frac{\pi h a^2}{E'}\Big(p^2 - \sigma_h^2\Big). \tag{18}$$

The energy function $W(a,p)$ can be used to compute the energy release by creating a new infinitesimal fracture surface area $dA = 2h\, da$. The factor 2 represents the two

surfaces of the line segment da. The energy needed to create the new fracture surface area is the surface energy γ given by

$$\frac{dW}{dA} = 2\gamma \tag{19}$$

which gives that

$$\frac{\pi a}{E'}\left(p^2 - \sigma_h^2\right) = 2\gamma \tag{20}$$

or the critical fluid pressure for a fracture with length a

$$p_c(a) = \left(\sigma_h + \frac{2\gamma E'}{\pi a}\right)^{1/2} \tag{21}$$

There are two useful approximations of $p_c(a)$, depending on the characteristic length

$$a_0 = \frac{\gamma E'}{\pi \sigma_h^2} \tag{22}$$

The critical fracture pressure can then be approximated as

$$p_c(a) = \sigma_h \cdot \left(1 + \frac{2a_0}{a}\right)^{1/2} = \begin{cases} \sigma_h \cdot (2a_0/a)^{1/2} & \text{for } a \ll a_0 \\ \sigma_h \cdot (1 + a_0/a) & \text{for } a \gg a_0 \end{cases} \tag{23}$$

in terms of the regimes defined by characteristic length a_0.

References

Adachi, J., Siebrits, E., Peirce, A., Desroches, J., 2007. Computer simulation of hydraulic fractures. International Journal of Rock Mechanics and Mining Sciences 44, 739–757. doi:10.1016/j.ijrmms.2006.11.006.

Alpak, F.O., Wheeler, M.F., 2012. A supercoarsening multigrid method for poroelasticity in 3d coupled flow and geomechanics modeling. Computational Geosciences 16, 953–974. doi:10.1007/s10596-012-9297-z.

Baisch, S., Voros, R., Rothert, E., Stang, H., Jung, R., Schellschmidt, R., 2010. A numerical model for fluid injection induced seismicity at soultz-sous-forłts. International Journal of Rock Mechanics and Mining Sciences 47, 405 – 413.

Charlez, P., 1997. Rocks Mechanics, Vol II. Petroleum applications. Édition Technip, Paris. chapter 6.

Dean, R.H., Schmidt, J.H., 2009. Hydraulic-fracture predictions with a fully coupled geomechanical reservoir simulator. SPE Journal 14, 707–714.

Flekkøy, E., Malthe-Sørenssen, A., Jamtveit, B., 2002. Modeling hydrofracture. Journal of Geophysical Research 107, ECV1–1–11.

Ganis, B., Mear, M.E., Sakhaee-Pour, A., Wheeler, M.F., Wick, T., 2014. Modeling fluid injection in fractures with a reservoir simulator coupled to a boundary element method. Computational Geosciences 18, 613–624.

Geertsma, J., de Klerk, F., 1969. A rapid method of predicting width and extent of hydraulically induced fractures. Journal of Petroleum Technology 21, 1571–1581.

Jaeger, J., Cook, N., Zimmerman, R., 2007. Fundamentals of rock mechanics, Forth edition. Blackwell Scientific Publications.

Ji, L. Settari, A., Sullivan, R., 2009. A novel hydraulic fracturing model fully coupled with geomechanics and reservoir simulation. Society of Petroleum Engineers Journal SPE 110845, 423–430.

Khristianovic, S., Zheltov, Y., 1955. Formation of vertical fractures by means of highly viscous liquid, in: Proceedings Fourth World Petroleum Congress, Rome, Rome, Italy. pp. 579–586.

Kim, J., Moridis, G.J., 2013. Development of the T+M coupled flow-geomechanical simulator to describe fracture propagation and coupled flow-thermal-geomechanical processes in tight/shale gas systems. Computers & Geosciences 60, 184 – 198.

Kim, J., Moridis, G.J., 2015. Numerical analysis of fracture propagation during hydraulic fracturing operations in shale gas systems. International Journal of Rock Mechanics and Mining Sciences 76, 127 – 137.

Kim, J., Tchelepi, H.A., Juanes, R., 2011a. Stability, accuracy and efficiency of sequential methods. Society of Petroleum Engineers SPE 119084, 1–20.

Kim, J., Tchelepi, H.A., Juanes, R., 2011b. Stability and convergence of sequential methods for coupled flow and geomechanics: Fixed-stress and fixed-strain splits. Computer Methods in Applied Mechanics and Engineering 200, 1591–1606. doi:10.1016/j.cma.2010.12.022.

Kovalyshen, Y., Detournay, E., 2010. A reexamination of the classical PKN model of hydraulic fracture. Transport in Porous Media 81, 317–339. doi:10.1007/s11242-009-9403-4.

Lawn, B., 1993. Fracture of Brittle Solids. Second ed., Cambridge University Press.

Lee, S., Wheeler, M., Wick, T., 2016. Pressure and fluid-driven fracture propagation in porous media using and adaptive finite element phase field model. Technical Report ICES Report 16-04. The Institute for Comnputational Engineering and Sciences, University of Texas, at Austin.

Mack, M.G., Warpinski, N.R., 2000. Mechanics of Hydraulic Fracturing. Wiley. chapter 6. Reservoir Stimulation, pp. 6.1–6.49.

Norbeck, J., Horne, R., 2014. An embedded fracture modeling framework for fluid flow, geomechanics, and fracture propagation, in: Proceedings of the International Conference on Discrete Fracture Network Engineering, DFNE, International

Discrete Fracture Network Engineering Conference, Vancouver, British Columbia, Canada. pp. 1–10.

Norbeck, J., McClure, M., Horne, R., 2016. An embedded fracture modeling framework for simulation of hydraulic fracturing and shear stimulation. Computational Geosciences 20, 1–18.

Nordgren, R., 1972. Propagation of a vertical hydraulic fracture. Society of Petroleum Engineers Journal SPE 3009, 306–314.

Norris, J.Q., Turcotte, D.L., Rundle, J.B., 2014. Loopless nontrapping invasion-percolation model for fracking. Phys. Rev. E 89, 022119. doi:10.1103/PhysRevE.89.022119.

Perkins, K., Kern, L., 1961. Widths of hydraulic fractures. Journal of Petroleum Technology 13, 937–949.

Riahi, A., Damjanac, B., 2013. Numerical study of hydro-shearing in geothermal reservoirs with a pre-existing discrete fracture network, in: Proceedings, Thirty-Eighth Workshop on Geothermal Reservoir Engineering, Stanford University, California. pp. 1–13.

Rutqvist, J., 2011. Status of the tough-flac simulator and recent applications related to coupled fluid flow and crustal deformations. Computers & Geosciences 37, 739–750.

Settari, T., Walters, D., 2001. Advances in coupled geomechanical and reservoir modelling with application to reservoir compaction. Society of Petroleum Engineers Journal 6, 334–342. doi:10.2118/51927-MS.

Shimizu, H., Murata, S., Ishida, T., 2011. The distinct element analysis for hydraulic fracturing in hard rock considering fluid viscosity and particle size distribution. International Journal of Rock Mechanics and Mining Sciences 48, 712 – 727.

Turcotte, D., Moores, E., Rundle, J., 2014. Super fracking. Physics Today 67, 34–39. doi:10.1063/PT.3.2480.

Tzschichholz, F., Herrmann, H., 1995. Simulations of pressure fluctuations and acoustic emission in hydraulic fracturing. Phys. Rev. E 51, 1961–1970.

Tzschichholz, F., Herrmann, H., Roman, H., M., P., 1994. Beam model for hydraulic fracturing. Phys. Rev. B 49, 7056–7059.

Tzschichholz, F., Wangen, M., 1998. Modelling of hydraulic fracturing of porous materials. WIT Press, Southhampton. pp. 227–260.

Wang, H., 2000. Theory of linear poroelasticity. Princeton University Press.

Wangen, M., 2010. Physical principles of sedimentary basin analysis. Cambridge University Press.

Wangen, M., 2011. Finite element modelling of hydraulic fracturing on a reservoir scale in 2d. Journal of Petroleum Science and Engineering 77, 274–285. doi:10.1016/j.petrol.2011.04.001.

Wangen, M., 2013. Finite element modeling of hydraulic fracturing in 3d. Computational Geosciences 17, 647–659. doi:10.1007/s10596-013-9346-2.

Wheeler, M., Wick, T., Wollner, W., 2014. An augmented-Lagrangian method for the phase-field approach for pressurized fractures. Computers Methods in Applied Mechanics and Engineering 271, 69–85.

Zoback, M.D., 2010. Reservoir geomechanics. Cambridge University Press.